Entanglement phase transitions in non-Hermitian Floquet systems

Longwen Zhou ●*

College of Physics and Optoelectronic Engineering, Ocean University of China, Qingdao 266100, China;
Key Laboratory of Optics and Optoelectronics, Qingdao 266100, China;
and Engineering Research Center of Advanced Marine Physical Instruments and Equipment of MOE, Qingdao 266100, China

The competition between unitary time evolution and quantum measurements could induce phase transitions in the entanglement characteristics of quantum many-body dynamics. In this work, we reveal such entanglement transitions in the context of non-Hermitian Floquet systems. Focusing on noninteracting fermions in a representative bipartite lattice with balanced gain/loss and under time-periodic quenches, we uncover rich patterns of entanglement transitions due to the interplay between driving and non-Hermitian effects. Specially, we find that the monotonic increase of quenched hopping amplitude could flip the system between volume-law and area-law entangled Floquet phases, yielding alternated entanglement transitions. Meanwhile, the increase of gain/loss strength could trigger area-law to volume-law reentrant transitions in the scaling behavior of steady-state entanglement entropy, which are abnormal and highly unexpected in nondriven systems. Connections between entanglement transitions and parity-time-reversal (PT) transitions in Floquet spectra are further established. Our findings not only build a foundation for exploring entanglement phase transitions in Floquet non-Hermitian setups, but also provide efficient means to engineer and control such transitions by driving fields.

I. INTRODUCTION

Non-Hermitian Floquet systems have attracted great interest in recent years (see Ref. [1] for a review). The interplay between periodic drivings and non-Hermitian effects were found to generate a great variety of phases and transitions with unique dynamical and topological features in insulating [2–18], superconducting [19–21], semimetallic [22–26], and quasicrystalline [27,28] systems. In experiments, non-Hermitian Floquet physics has also been explored in various steps including photonics [29–34], acoustics [35,36], electrical circuits [37,38], and ultracold atoms [39–42], yielding potential applications in stabilizing topological states and controlling material features in open systems.

Despite constant progress, the entanglement properties of non-Hermitian Floquet matter are much less explored. As an intriguing phenomenon of entanglement dynamics, the measurement-induced phase transitions have garnered increasing attention since 2018 [43–50]. It was found that with the increase of measurement rates, the steady-state entanglement entropy (EE) of a quantum many-body system could undergo a volume-law to area-law transition in its scaling behavior versus the system size, which is originated from the competition between unitary dynamics and projective measurements [51–53]. Recently, such entanglement phase transitions have also been explored in the context of non-Hermitian physics [54–63], where the development of a dissipation gap and the presence of non-Hermitian skin effects (NHSEs) were identified as typical mechanisms of generating these transitions. As PT-symmetry breaking in the spectrum [2] and NHSEs [12] can both be flexibly controlled by time-periodic driving fields, much richer patterns of entanglement phase transitions are expected to emerge in Floquet non-Hermitian systems compared with the static case. Furthermore, the interplay between drivings and non-Hermitian effects may lead to unique types of entanglement transitions that are absent in nondriven situations, which have yet to be revealed.

In this work, we address these issues by exploring entanglement phase transitions in non-Hermitian Floquet systems. In Sec. II, we introduce one minimal model of non-Hermitian Floquet system, which corresponds to a periodically quenched Su-Schrieffer-Heeger (SSH) [64,65] model with balanced gain and loss on different sublattices. We analytically obtain the Floquet spectrum of our model and discover rich patterns of PT transitions induced by driving and non-Hermitian effects. In Sec. III, we reveal diversified entanglement phase transitions in our model and establish the entanglement phase diagrams by investigating the scaling law of steady-state EE versus the system size following long-time stroboscopic evolutions. In Sec. IV, we summarize our results, comment on issues related to experiments and discuss potential future directions. The numerical method we adopted to study entanglement dynamics of non-Hermitian Floquet systems is sketched in Appendix A. Entanglement transitions in a generalized version of our model are briefly discussed in the Appendix B.
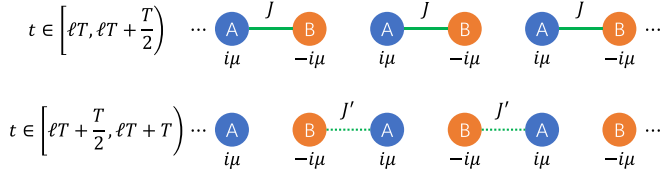
*zhoulw13@u.nus.edu

FIG. 1. Schematic diagram of a periodically quenched non-Hermitian SSH (NHSSH) model. The chains in the first and second rows denote the systems in the first and the second half of a driving period T. $\ell \in \mathbb{Z}$ and t denotes time. J and J' are the intracell and intercell hopping amplitudes. Balanced gain ($i\mu$) and loss ($-i\mu$) are acted on the sublattices A and B. In our calculations, we introduce real dimensionless parameters $J_1 \equiv JT/(2\hbar)$, $J_2 \equiv J'T/(2\hbar)$, and $\gamma \equiv \mu T/(2\hbar)$ for the hopping amplitudes and gain/loss strength.

II. MODEL AND FLOQUET SPECTRUM

To demonstrate the entanglement transitions in non-Hermitian Floquet systems, we focus on a periodically quenched SSH model with balanced gain and loss. A schematic illustration of the model is shown in Fig. 1. The SSH model forms a paradigmatic setup in the study of topological insulators. It owns two sublattices A and B within each unit cell and possesses dimerized hopping amplitudes among adjacent lattice sites. In our driving scheme, the intracell and intercell hopping terms of the SSH model are switched on and off alternatively within each temporal modulation period. The gain and loss are time independent and acting locally on the sublattices A and B, respectively. The Floquet operator of the system, which describes its evolution over a complete driving period is given by

$$\hat{U} = e^{-i\hat{H}_2} e^{-i\hat{H}_1}, \tag{1}$$

where

$$\hat{H}_1 = J_1 \sum_n (\hat{c}_{n,A}^\dagger \hat{c}_{n,B} + \text{H.c.}) + i\gamma \sum_n (\hat{c}_{n,A}^\dagger \hat{c}_{n,A} - \hat{c}_{n,B}^\dagger \hat{c}_{n,B}), \tag{2}$$

$$\hat{H}_2 = J_2 \sum_n (\hat{c}_{n,B}^\dagger \hat{c}_{n+1,A} + \text{H.c.}) + i\gamma \sum_n (\hat{c}_{n,A}^\dagger \hat{c}_{n,A} - \hat{c}_{n,B}^\dagger \hat{c}_{n,B}). \tag{3}$$

Here $\hat{c}_{n,s}^\dagger$ ($\hat{c}_{n,s}$) creates (annihilates) a fermion on the sublattice s ($= A, B$) in the nth unit cell. Applying the Fourier transformations $\hat{c}_{n,s} = \frac{1}{\sqrt{L}} \sum_k e^{ikn} \hat{c}_{k,s}$ for $s = A, B$ to the system with L unit cells under the PBC, we can express $\hat{H}_1$ and $\hat{H}_2$ in the momentum space as $\hat{H}_1 = \sum_k \hat{C}_k^\dagger H_1(k) \hat{C}_k$ and $\hat{H}_2 = \sum_k \hat{C}_k^\dagger H_2(k) \hat{C}_k$, where $\hat{C}_k^\dagger \equiv (\hat{c}_{k,A}^\dagger, \hat{c}_{k,B}^\dagger)$,

$$H_1(k) = J_1 \sigma_x + i\gamma \sigma_z, \tag{4}$$

$$H_2(k) = J_2 \cos k \sigma_x + J_2 \sin k \sigma_y + i\gamma \sigma_z. \tag{5}$$

$\sigma_{x,y,z}$ are Pauli matrices in their usual representations. $k \in [-\pi, \pi)$ denotes the quasimomentum. The associated Floquet operator then reads

$$\hat{U} = \sum_k \hat{C}_k^\dagger U(k) \hat{C}_k, \quad U(k) = e^{-iH_2(k)} e^{-iH_1(k)}. \tag{6}$$

It is not hard to justify that the Bloch Hamiltonians $H_1(k)$ and $H_2(k)$ both possess the PT symmetry, i.e., $[\mathcal{PT}, H_1(k)] = [\mathcal{PT}, H_2(k)] = 0$, with the parity $\mathcal{P} = \sigma_x$ and the time reversal $\mathcal{T} = \mathcal{K}$, where $\mathcal{K}$ takes the complex conjugate. Therefore, the Bloch-Floquet operator $U(k)$, when expressed in a symmetric time frame as

$$\mathcal{U}(k) = e^{-\frac{i}{2}H_1(k)} e^{-iH_2(k)} e^{-\frac{i}{2}H_1(k)}, \tag{7}$$

also possesses the PT symmetry in the sense that

$$\mathcal{PT}\mathcal{U}(k)\mathcal{PT} = \mathcal{U}^{-1}(k). \tag{8}$$

The quasienergy spectrum of $\mathcal{U}(k)$ could thus be real in certain parameter domains even though $\mathcal{U}(k)$ is not unitary. Since $U(k)$ and $\mathcal{U}(k)$ are related by a similarity transformation that does not affect the spectrum, the original system described by $U(k)$ could also have a real quasienergy spectrum in the same parameter regions as of $\mathcal{U}(k)$. Therefore, our periodically quenched NHSSH model holds the PT symmetry and its quasienergy spectrum may undergo real-to-complex transitions with the increase of the gain and loss strength γ. The Floquet spectrum of our system can be obtained by solving the eigenvalue equation $U(k)|\psi\rangle = e^{-iE(k)}|\psi\rangle$. The resulting quasienergy dispersions take the forms $E_\pm(k) = \pm E(k)$, with

$$E(k) = \arccos(\cos E_1 \cos E_2 - \mathbf{n}_1 \cdot \mathbf{n}_2 \sin E_1 \sin E_2). \tag{9}$$

Here the terms $E_1 = \sqrt{J_1^2 - \gamma^2}$, $E_2 = \sqrt{J_2^2 - \gamma^2}$, $\mathbf{n}_1 = (J_1, 0, i\gamma)/E_1$, and $\mathbf{n}_2 = (J_2 \cos k, J_2 \sin k, i\gamma)/E_2$. From Eq. (9), it is not hard to verify that $\cos[E(k)]$ is always real. Therefore, when $|\cos[E(k)]| < 1$ for all k, the quasienergy dispersions $\pm E(k)$ must be purely real and the system resides in the PT-invariant regime. When $|\cos[E(k)]| > 1$ for certain k, the $\pm E(k)$ must be complex and the system goes into a PT-broken phase. A PT transition in the system is then expected to happen at $\cos[E(k)] = \pm 1$, or

$$\cos E_1 \cos E_2 - \mathbf{n}_1 \cdot \mathbf{n}_2 \sin E_1 \sin E_2 = \pm 1. \tag{10}$$

Note that these are also the conditions for the two Floquet bands $E_\pm(k)$ to touch with each other at the center ($E = 0$, $\cos[E(k)] = 1$) and boundary ($E = \pi$, $\cos[E(k)] = -1$) of the first quasienergy Brillouin zone (BZ) $\text{Re}E \in (-\pi, \pi]$, respectively. These touching points are second-order Floquet exceptional points (FEPs). In the first BZ of k, they appear at the quasimomenta $\pm k_c$ that satisfy $k_c = \arccos[\frac{1}{J_1 J_2}(\frac{\cos E_1 \cos E_2 - 1}{\sin E_1 \sin E_2} E_1 E_2 + \gamma^2)]$ with $E(k_c) = 0$ and $k_c = \arccos[\frac{1}{J_1 J_2}(\frac{\cos E_1 \cos E_2 + 1}{\sin E_1 \sin E_2} E_1 E_2 + \gamma^2)]$ with $E(k_c) = \pi$, respectively. Note that the FEPs emerging at the boundary of Floquet BZ ($E = \pi$) are unique to non-Hermitian Floquet systems. Similar to exceptional points of static Hamiltonians [66], FEPs could also lead to the breakdown of adiabatic predictions in driven systems.

In Fig. 2, we present typical cases of the Floquet spectrum $E_\pm(k)$ [Eq. (9)] for our periodically quenched NHSSH model under PBC. We find that with the change of the hopping or gain and loss parameter, the line quasienergy gap between the two Floquet bands could close at either $E = 0$ or $E = \pi$, which is followed by the change of spectral compositions (real, purely complex or partially real). We thus expect to have both PT breaking and restoring transitions in the system, which are clearly illustrated by the panels at different
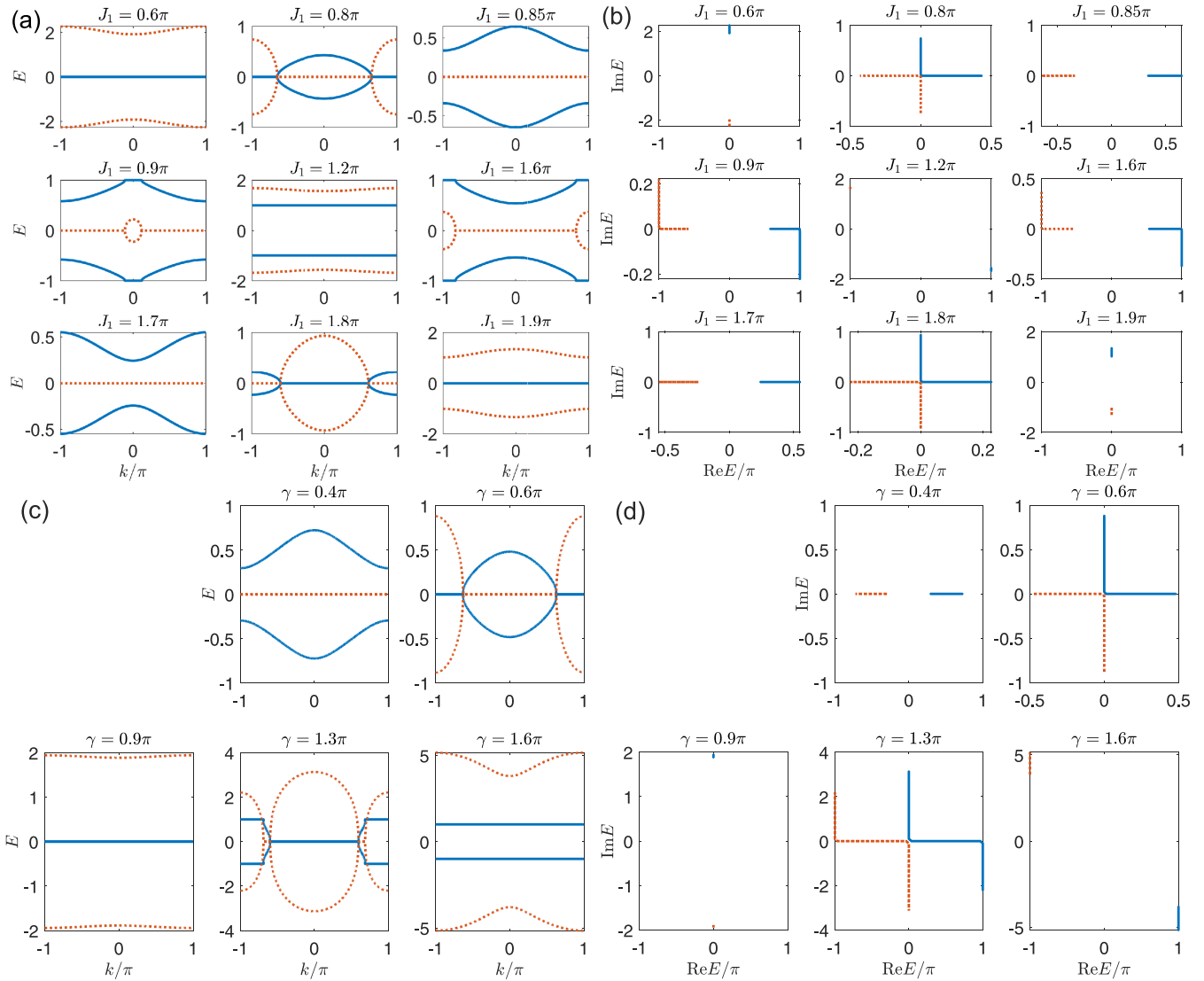
FIG. 2. Floquet quasienergy spectrum of the periodically quenched NHSSH model under PBC. Other system parameters are $(J_2, \gamma) = (0.1\pi, 0.5\pi)$ for (a), (b) and $(J_1, J_2) = (2.2\pi, 2\pi/3)$ for (c), (d). In (a) and (c), the blue solid and red dotted lines denote $\pm \mathrm{Re} E(k)/\pi$ and $\pm \mathrm{Im} E(k)$ vs the quasimomentum k. In (b) and (d), the blue solid and red dotted lines represent the two Floquet bands $\pm E$ on the complex quasienergy plane.

J_1 in Figs. 2(a) and 2(b). Moreover, we observe that with the increase of γ, the Floquet spectrum does not change monotonically from real to purely complex. It could instead enter an intermediate phase with both real and complex quasienergies, as illustrated by the case with $\gamma = 1.3$ in Figs. 2(c) and 2(d). These rich spectral patterns, as identifiable from Fig. 2, clearly distinguish our Floquet model from its static non-Hermitian counterpart [59]. They also underline the alternated and reentrant entanglement transitions we are going to reveal in the next section.

To further characterize the composition of Floquet spectrum and discriminate between the PT-invariant and PT-broken phases, we introduce the ratio of real quasienergies of $U(k)$, which is defined as

$$R = \int_{-\pi}^{\pi} \frac{dk}{2\pi} \Theta(1 - |\cos[E(k)]|). \quad (11)$$

Here $\Theta(x)$ is the step function, which is equal to 1 (0) if $x > 0$ ($x < 0$). It is clear that we have $R = 1$ ($R = 0$) if all the quasienergies of $U(k)$ are real (complex). If $R \in (0, 1)$, real and complex quasienergies coexist in the Floquet spectrum of $U(k)$. A PT-breaking transition then happens when the value of R starts to decrease from one. In Fig. 3, we present the quasienergy spectrum [Eq. (9)] and the real-quasienergy ratio [Eq. (11)] versus the hopping amplitude J_1 and the gain/loss strength γ separately for our periodically quenched NHSSH model. A series of alternated PT-breaking ($R = 1 \rightarrow R < 1$) and PT-restoring ($R < 1 \rightarrow R = 1$) transitions can be observed with the change of J_1. These transitions are accompanied by band touchings at the quasienergy zero or π. They are further mediated by critical phases with coexisting real and complex quasienergies ($0 < R < 1$) in the Floquet spectrum. Meanwhile, we notice that with the raise of γ from zero, the system could first undergo a PT-breaking
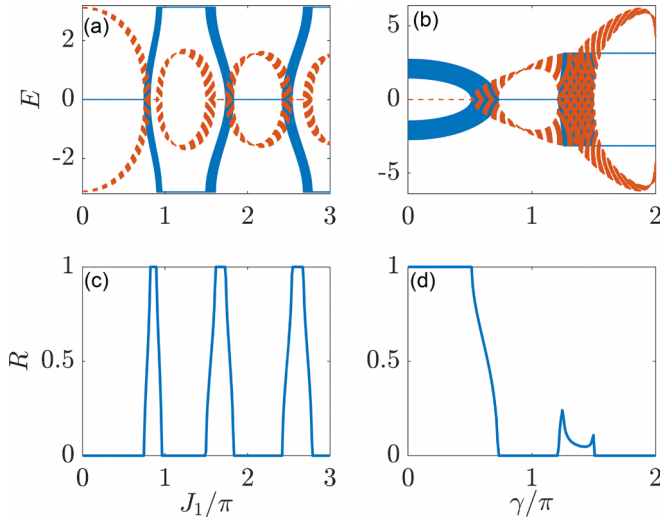
FIG. 3. Floquet spectrum E [(a), (b)] and ratios of real quasienergies R [(c), (d)] vs the hopping amplitude J_1 and gain/loss parameter γ under the PBC. Other system parameters are $(J_2, \gamma) = (0.1\pi, 0.5\pi)$ for (a), (c) and $(J_1, J_2) = (2.2\pi, 2\pi/3)$ for (b), (d). The solid and dashed lines in (a) and (b) denote the real and imaginary parts of quasienergy.

FIG. 4. Ratios of real quasienergies R [Eq. (11)] versus (a) (J_1, J_2) at $\gamma = \pi/2$ and (b) (J_1, γ) at $J_2 = 2\pi/3$ for the periodically quenched NHSSH model [Eq. (1)] under PBC. Different colors represent different values of R, as can be read out from the color bars.

III. ENTANGLEMENT PHASE TRANSITIONS

In static non-Hermitian systems, it has been identified that the opening of a dissipation gap along the imaginary-energy axis could lead to a volume-law to area-law phase transition in the EE of free fermions [59]. The non-Hermitian skin effect constitutes another mechanism of generating such entanglement phase transitions [57]. The presence of random or quasiperiodic disorder may further collaborate with non-Hermitian effects to generate anomalous log-law to area-law entanglement transitions [62]. Beyond these static situations, we will now demonstrate how entanglement phase transitions could be induced and controlled by time-periodic drivings in our non-Hermitian Floquet system.

We first outline the methodology of obtaining the EE and its stroboscopic dynamics for noninteracting fermions in a Floquet non-Hermitian lattice. Let us consider a system initialized in the state $|\Psi_0\rangle$ at time $t = 0$ and evolved by the Floquet operator $\hat{U}$ with the driving period T. The normalized state of the system after a number of ℓ ($\in \mathbb{N}$) driving periods is given by

$$|\Psi(\ell T)\rangle = \frac{\hat{U}^\ell |\Psi_0\rangle}{\sqrt{\langle \Psi_0 | \hat{U}^{\dagger\ell} \hat{U}^\ell | \Psi_0\rangle}}. \tag{12}$$

Note in passing that for a non-Hermitian Floquet system, we usually have $\hat{U}^\dagger \hat{U} \neq 1$, and the resulting stroboscopic dynamics is not unitary. Physically, the renormalization process in Eq. (12) can be related to open-system dynamics dependent on measurement outcomes, so that the quantum evolution corresponds to the null-jump process [57,59,67–70]. Over each driving period, the state evolves following the Schrödinger equation with an effective non-Hermitian Hamiltonian $\hat{H} = i\ln\hat{U}$. This is followed by a normalization of the wave function without going through quantum jumps (postselection).

In the absence of gain and loss ($\gamma = 0$), the Hamiltonians $\hat{H}_1$ and $\hat{H}_2$ of our system in the two halves of its evolution period are both Hermitian, and the resulting Floquet dynamics as described by $\hat{U}$ [Eq. (1)] is strictly unitary. In this case, the denominator of Eq. (12) is always one for a normalized $|\Psi_0\rangle$, and there are no issues concerning the exponential growth of amplitude of the evolving state $\hat{U}^\ell |\Psi_0\rangle$. With finite gain and loss ($\gamma \neq 0$), the Floquet spectrum of $\hat{U}$ may become fully complex or partially complex with second-order FEPs (see Fig. 2) under PBC. In this case, the norm of the evolved state $\hat{U}^\ell |\Psi_0\rangle$ may become larger than one and even grow exponentially before the renormalization operated in Eq. (12). Possible

transition and its Floquet spectrum changes gradually from partially real to purely complex. However, real quasienergies could reappear in a region with larger γ, which is rarely achievable with the raise of gain and loss strengths in static non-Hermitian systems. These reentrant PT transitions and gain/loss-induced real quasienergies are both originated from the interplay between drivings and non-Hermitian effects. Their notable influences on entanglement phase transitions in our non-Hermitian Floquet system will be revealed in Sec. III. In Fig. 4, we show the values of R versus (J_1, J_2) and (J_1, γ) as two typical cases of PT phase diagrams under the PBC. In both Figs. 4(a) and 4(b), we observe rich patterns of PT-invariant (in dark red), PT-broken (in dark blue), and intermediate ($0 < R < 1$) phases with different compositions of the Floquet spectrum. Moreover, the change of each system parameter could induce a series of alternated and reentrant PT transitions in the spectrum, which is usually unavailable in static non-Hermitian systems. Specially, we find that with the increase of gain and loss strength γ, the spectrum could first change gradually from real ($R = 1$) to purely complex ($R = 0$), and then going back to a mixed case ($0 < R < 1$) with coexisting real and complex quasienergies [Fig. 4(b)]. This is again unexpected in static non-Hermitian systems, where a stronger gain and loss usually prefer a larger proportion of complex eigenenergy in the spectrum. These observations imply that time-periodic driving fields could not only induce rich PT phases and transitions, but also provide a mechanism to stabilize PT-symmetric non-Hermitian systems in stronger dissipation regions.

In the next section, we will characterize the entanglement nature of Floquet phases with different spectral properties in our periodically quenched NHSSH model. The rich and alternated spectrum transitions found here will be further related to reentrant entanglement transitions in our system.
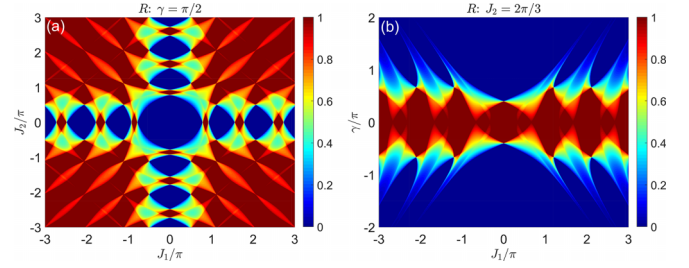
issues related to this exponential growth of state's amplitude can be resolved by adding to our system a time-independent global loss term in the form of $-i\Gamma \sum_n (\hat{c}_{n,A}^\dagger \hat{c}_{n,A} + \hat{c}_{n,B}^\dagger \hat{c}_{n,B})$, where the loss rate $\Gamma > 0$ can be chosen to be large enough. In this case, the norm of the evolving state $\hat{U}^\ell |\Psi_0\rangle$ can only decay over time. Meanwhile, the dynamics described by our Eq. (12) is unaffected, as the global loss terms in the numerator and denominator would be canceled.

In our numerical calculations, we take the PBC and choose the initial state as

$$|\Psi_0\rangle = \prod_{n=1}^{L} \hat{c}_{n,B}^\dagger |\varnothing\rangle. \tag{13}$$

Here L is the total number of unit cells in the lattice and $|\varnothing\rangle$ denotes the vacuum state. The state $|\Psi_0\rangle$ in Eq. (13) thus describes a charge density wave at half-filling, with each sublattice B being populated by a single fermion. This initial state is not an eigenstate of the Floquet operator $\hat{U}$ [Eq. (1)] or the noncommutative Hamiltonians $\hat{H}_{1,2}$ [Eqs. (2)–(3)]. The system's hopping parameters will experience sudden changes in the middle of each driving period, and there are no slowly varying parameters. Therefore, our system will undergo far-from-equilibrium dynamics and reaching some steady states after being evolved stroboscopically over multiple driving periods. Such a process is nonadiabatic and thus could not be captured by adiabatic predictions. Other types of pure and nonequilibrium initial states yield consistent results concerning the entanglement transitions that will be studied below.

At any stroboscopic time $t = \ell T$, the matrix elements of single-particle correlator $C(\ell T)$ in the lattice representation can now be expressed as

$$C_{ms,m's'}(\ell T) = \langle \Psi(\ell T)|\hat{c}_{m,s}^\dagger \hat{c}_{m',s'}|\Psi(\ell T)\rangle, \tag{14}$$

where $m, m' = 1, \ldots, L$ and $s, s' = A, B$ denote the unit cell and sublattice indices, respectively. Restricting the indices m, m' of $C(\ell T)$ to a subsystem X with l unit cells gives us a $2l \times 2l$ block of $C(\ell T)$. The eigenvalues of this block constitute the correlation-matrix spectrum $\{\zeta_j(\ell T)|j = 1, \ldots 2l\}$ of the subsystem X. Without interactions, the $|\Psi(t)\rangle$ is a Gaussian state and the bipartite EE can be obtained from the spectrum of correlation matrix [71]. That is, at any given stroboscopic time $t = \ell T$, we can find the EE between the subsystem X and remaining part Y of the whole system as

$$S(t) = -\sum_{j=1}^{2l} [\zeta_j \ln \zeta_j + (1 - \zeta_j) \ln(1 - \zeta_j)]. \tag{15}$$

Here we have suppressed the time dependence in ζ_j for brevity. The $S(t)$ thus defined corresponds to the bipartite EE $S(t) = -\mathrm{Tr}[\rho_X(t) \ln \rho_X(t)]$, where the reduced density matrix $\rho_X(t)$ of subsystem X can be obtained by tracing out all the degrees of freedom belonging to the remaining subsystem Y with $2(L - l)$ sites, i.e., $\rho_X(t) = \mathrm{Tr}_Y[|\Psi(t)\rangle\langle\Psi(t)|]$. The numerical recipe of computing the single-particle correlation matrix and EE for a non-Hermitian Floquet system are summarized in Appendix A. We emphasize that our approach only uses the right vector of a single wave function, instead of biorthogonal density matrices constructed from both right and left eigenstates. We first investigate the scaling behaviors
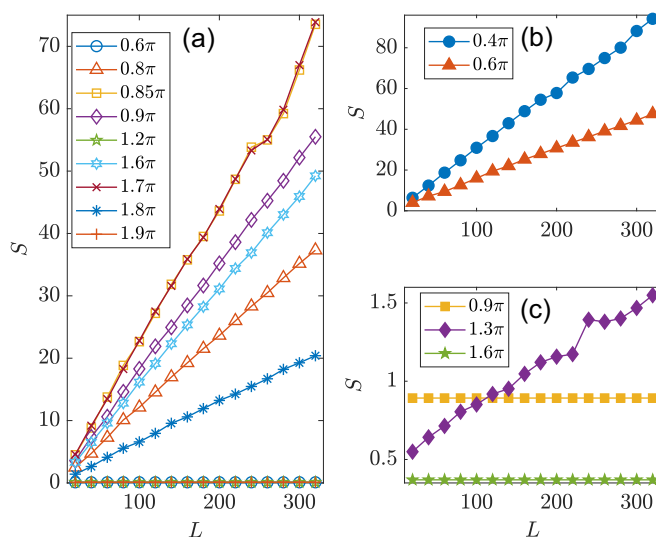

FIG. 5. Steady-state EE $S(L, l)$ versus the system size L under PBC for a equal bipartition $l = L/2$ and at half-filling. In (a), the legend gives the value of J_1 for each curve, with other system parameters given by $(J_2, \gamma) = (0.1\pi, 0.5\pi)$ [same as those taken in Figs. 2(a) and 2(b)]. In (b) and (c), the legends show the value of γ for each curve, with other system parameters given by $(J_1, J_2) = (2.2\pi, 2\pi/3)$ [same as those used in Figs. 2(c) and 2(d)].

of steady-state EE $S(L, l)$ vs the system size L for $l = L/2$ (equal bipartition), at half-filling and under PBC. For a given L and l, $S(L, l)$ is obtained by averaging the stroboscopic EE $S(t)$ [Eq. (15)] over a late-time domain $t \in [\ell' T, \ell T]$ with $1 \ll \ell' < \ell$, where we take $\ell' = 800$ and $\ell = 1000$ throughout our numerical calculations. In Fig. 5, we observe two drastically distinct scaling behaviors in $S(L, L/2)$ at different strengths of hopping J_1 [Fig. 5(a)] and gain/loss γ [Figs. 5(b)–5(c)]. Referring to Fig. 2, we realize that whenever the Floquet spectrum of our periodically quenched NHSSH model forms a dissipation gap along the imaginary-quasienergy axis, the steady-state EE becomes independent of the system size L in Fig. 5, such that $S(L, L/2) \sim L^0$ and area-law scalings are observed in associated cases. Instead, in the cases when imaginary quasienergy gaps vanish in Fig. 2, the steady-state EE becomes proportional to the system size L in Fig. 5, such that volume-law entangled phases with $S(L, L/2) \sim L$ are reached.

Note in passing that within the volume-law entangled phases, the gradients of $S(L, L/2)$ versus L reach maximal values in PT-invariant cases with real quasienergy spectra [for $J_1 = 0.85\pi, 1.7\pi$ in Fig. 5(a) and $\gamma = 0.4\pi$ in Fig. 5(b)]. Meanwhile, volume-law scalings of the steady-state EE can be observed in both PT-invariant and PT-broken phases, so long as there are no dissipation gaps along the imaginary quasienergy axis. These observations indicate that PT transitions do not have one-to-one correspondences with entanglement transitions in non-Hermitian Floquet systems. As another notable result, the scaling behavior of $S(L, L/2)$ changes from area-law to volume-law when the gain and loss strength γ raises from 0.9π to 1.3π in Fig. 5(c), which goes beyond the situation normally expected in nondriven systems. To further decode entanglement phase transitions
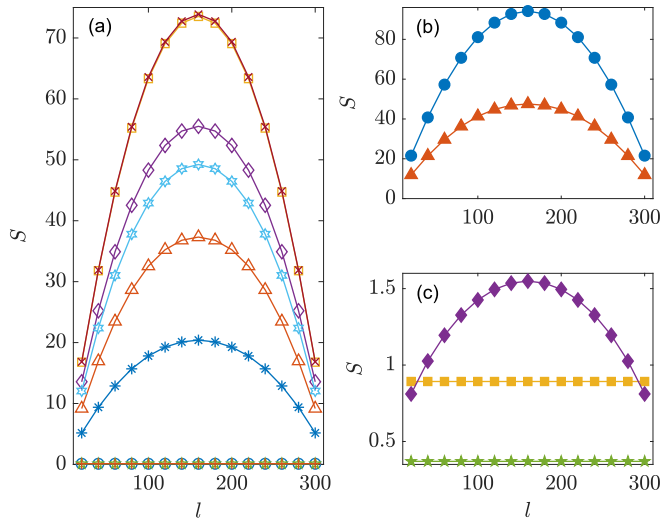
FIG. 6. Steady-state EE $S(L, l)$ versus the subsystem size l under PBC for a fixed total system size $L = 320$ and at half-filling. (a)–(c) share the same legends with the corresponding panels (a)–(c) of Fig. 5. The curves marked by the same symbol in Figs. 5 and 6 have the same system parameters.

in our non-Hermitian Floquet setting, we present in Fig. 6 the steady-state EE $S(L, l)$ versus the subsystem size l with a fixed total number of unit cells $L = 320$. The system is

still at half-filling and under PBC. In Figs. 6(a) and 6(c), we observe area-law scalings $S(L, l) \sim l^0$ in the steady-state EE for the cases with finite dissipation gaps along imaginary quasienergy axes of the Floquet spectra in Fig. 2. When imaginary quasienergy gaps vanish in Fig. 2, we find that the $S(L, l)$ in Figs. 6(a)–6(c) might be fitted by the function $g_0 \sin(\pi l/L) + g_1 \ln[\sin(\pi l/L)] + g_2$, which is usually expected in volume-law entangled phases. Therefore, the scaling behaviors of steady-state EE versus the subsystem size again suggest two possible phases with different entanglement nature in our periodically quenched NHSSH model, which are consistent with those observed in Fig. 5. We also notice that the appearance of these distinct entangling phases does not follow a monotonic sequence with the increase of either the quenched hopping amplitude J_1 or the gain and loss strength γ.

We are now ready to demonstrate entanglement phase transitions in our system. In Figs. 7(a) and 7(b), we present the steady-state EE $S(L, l = L/2)$ of our periodically quenched NHSSH model versus J_1 and γ, respectively, for several different system sizes L under the PBC and at half-filling. Two clearly distinct regions are observed in both figures. Referring to the spectrum information shown in Fig. 3, we conclude that in the parameter regions with gapped Floquet spectra along the imaginary quasienergy axis and $R = 0$, the steady-state EE follows an area-law scaling $S(L, L/2) \propto L^0$. Meanwhile, in the regions with $R \in (0, 1]$ and gapless Floquet
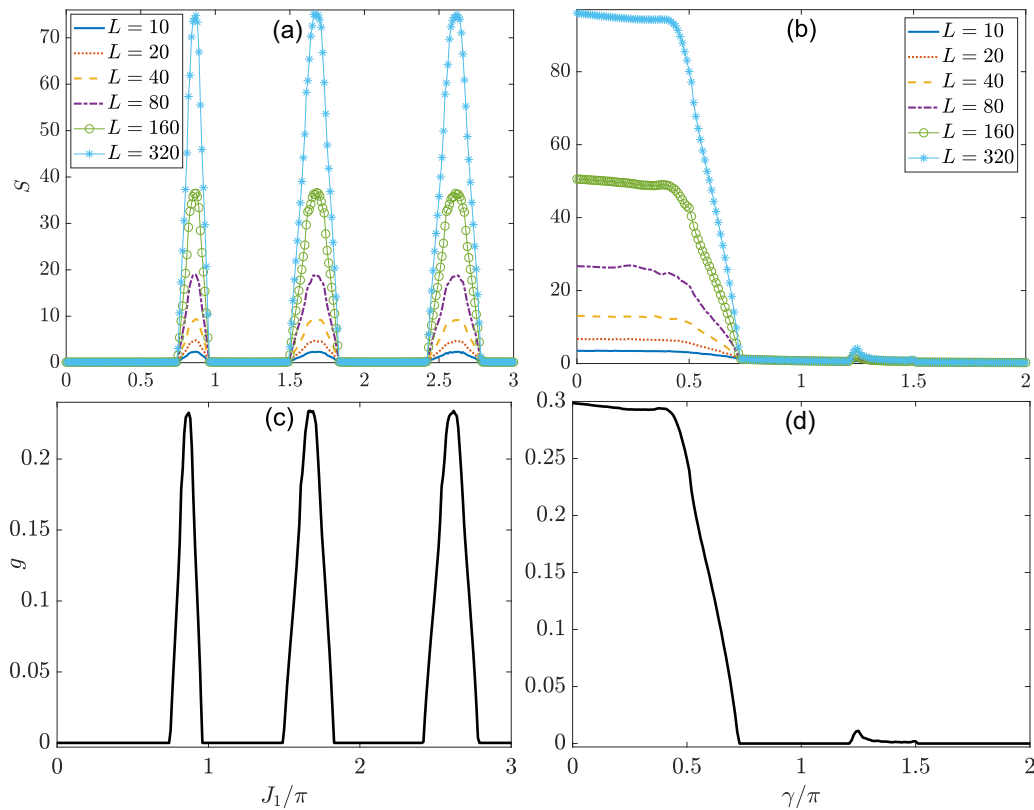

FIG. 7. Reentrant entanglement transitions versus the hopping amplitude J_1 [(a), (c)] and gain/loss strength γ [(b), (d)]. System parameters are $(J_2, \gamma) = (0.1\pi, 0.5\pi)$ for (a), (c) and $(J_1, J_2) = (2.2\pi, 2\pi/3)$ for (b), (d), which are the same as those chosen for the panels (a), (c) and (b), (d) of Fig. 3, respectively. (a) and (b) show the steady-state EE $S(L, l)$, with $l = L/2$, versus J_1 and γ for different lattice sizes L. (c) and (d) show the gradients g extracted from the linear fitting $S(L, L/2) \sim gL + s_0$.

spectra along the imaginary axis, the steady-state EE follows a volume-law scaling $S(L, L/2) \propto L$. Therefore, there should be entanglement transitions between volume-law entangled and area-law entangled phases with the change of hopping or gain/loss strength in our Floquet system. To confirm these entanglement transitions, we present in Figs. 7(c) and 7(d) the gradient g of steady-state EE, as obtained from the linear fitting $S(L, L/2) \sim gL + s_0$, versus J_1 and γ. Multiple area-law to volume-law (with $g = 0 \rightarrow > 0$) and volume-law to area-law (with $g > 0 \rightarrow = 0$) entanglement phase transitions are now clearly observable. Two notable features deserve to be further emphasized.

First, with the increase of quenched intracell hopping amplitude J_1 from zero, we find a series of alternated transitions between volume-law entangled and area-law entangled phases [Fig. 7(c)]. Similar patterns of alternated entanglement transitions can be obtained with the variation of intercell hopping amplitude J_2 when J_1 is fixed. Therefore, we could induce and even engineer entanglement phase transitions with high flexibility in non-Hermitian Floquet systems by tuning a single control parameter, which are hardly achievable in nondriven situations. The underlying physical picture is as follows. Since the real part of quasienergy is a phase factor and defined modulus 2π, two quasienergy bands of a non-Hermitian Floquet system could meet with each other and separate again at both $E = 0$ (center of the first quasienergy BZ) and $E = \pi$ (edge of the first quasienergy BZ). Moreover, due to the 2π-periodicity of E, the values of Floquet quasienergies E mod 2π in general could not change monotonically with the increase or decrease of a single system parameter. The combination of these two mechanisms then allows the Floquet bands of our system to touch and re-separate along the ImE axis sequentially at Re$E = 0$ and Re$E = \pi$. The final results are alternated entanglement phase transitions triggered by a single driving parameter, as observed in Fig. 7(c).

Second, with the increase of gain/loss amplitude γ, the system could first undergo a volume-law to area-law entanglement transition, which is followed by reentering a volume-law entangled phase through another entanglement transition at a larger γ, and finally going back to a area-law entangled phase with the further raise of γ [Fig. 7(d)]. Here, the non-Hermiticity-induced reentrant transition from area-law entangled to volume-law entangled phases is abnormal and usually not available in static non-Hermitian systems. As the real part of quasienergy also depends on γ, the reentrant entanglement transition observed here is due to the presence of two possible gap-closing points at $E = 0$ and π, the 2π periodicity of ReE and the nonmonotonous dependence of Floquet spectrum compositions on γ. Assisted by Floquet drivings, the re-emerged volume-law entangled phase at large dissipation rates may provide us with further room for protecting quantum information against decoherence. For completeness, we present in Fig. 8 the gradient g extracted from the linear fitting $S(L, L/2) \sim gL + s_0$ of the steady-state EE versus L at different system parameters, which constitutes the entanglement phase diagram of our periodically quenched NHSSH model. A comparison between Figs. 4 and 8 yield a nice consistency, i.e., the regions with $R = 0$ (fully complex Floquet spectra with finite dissipation gaps along ImE) and $R > 0$ (partially complex or real Floquet spectra with no

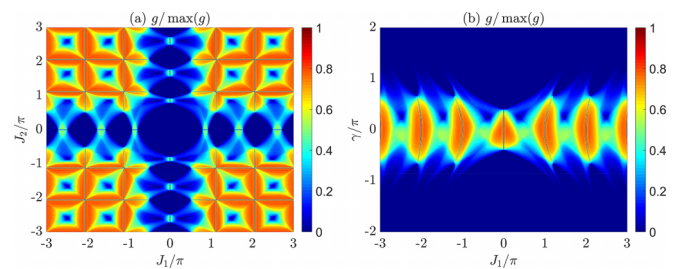FIG. 8. Entanglement phase diagrams vs (J_1, J_2) and (J_1, γ). Other system parameters are $\gamma = 0.5\pi$ for (a) and $J_2 = 2\pi/3$ for (b). The gradient g is obtained from the linear fitting $S(L, l) \sim gL + s_0$ of the steady-state EE with $l = L/2$ at half-filling and under PBC. The max(g) denotes the maximum of g over the considered parameter space $(J_1, J_2) \in (-3\pi, 3\pi) \times (-3\pi, 3\pi)$ [$(J_1, \gamma) \in (-3\pi, 3\pi) \times (-2\pi, 2\pi)$] in (a) [(b)].

dissipation gaps) are associated with area-law entangled and volume-law entangled phases, respectively. Moreover, rich patterns of entanglement phase transitions are observable over broad regions in the hopping and gain/loss parameter spaces. Therefore, we conclude that the interplay between periodic driving and non-Hermitian effects could not only generate rich phases with different entanglement nature, but also trigger alternated and reentrant entanglement transitions in examplary non-Hermitian Floquet systems.

In Appendix B, we briefly discussed a model following a different driving protocol, in which the intracell and intercell hopping terms are both present within each half of the driving period. Alternated and reentrant entanglement transitions are also found for the system considered there, whose features are qualitatively the same as those reported in our main text.

IV. CONCLUSION AND DISCUSSION

In this work, we applied the idea of Floquet engineering to generate and control entanglement phase transitions in non-Hermitian systems. By applying time-periodic quenches to the hopping amplitudes of fermions in a prototypical SSH model with balanced gain and loss, we found alternated and reentrant entanglement transitions due to the combined efforts of Floquet driving and non-Hermitian effects. System-size scaling behaviors of steady-state EE were systematically analyzed and entanglement phase diagrams were formulated for our considered model. The alternated transitions between volume-law and area-law entangled phases are due to driving-induced consecutive closings and reopenings of Floquet dissipation gaps along the imaginary quasienergy axis. The driving field also allows the composition of Floquet spectrum (real vs complex) to change nonmonotonically with the increase of gain and loss strengths, yielding abnormal area-law to volume-law reentrant transitions in the steady-state EE following the increase of non-Hermitian effects. The alternated and reentrant entanglement transitions found here are expected to be generic and observable in other driven non-Hermitian systems. Our work thus unveiled the diversity and richness of entanglement phase transitions in non-Hermitian Floquet systems. It further provided a flexible route to induce and control entanglement phase transitions in open systems via periodic driving fields.

Some remarks on the construction of our model and its experimental relevance are in order. First, in the early work of measurement-induced entanglement transitions [43–45], a hybrid quantum circuit with a brick-wall structure in space time was considered as a prototypical setup. That system consists of a one-dimensional (1D) spin-1/2 (or qubit) chain with nearest-neighbor gates. Every discrete time period of the circuit has two layers. Each layer has $L/2$ gates, operating on the odd links in the first layer and the even links in the second layer (see the Fig. 1 of Ref. [43]). From the perspective of Floquet system, the model considered in Ref. [43] may be viewed as a spin-1/2 chain whose nearest-neighbor spin-spin couplings are switched on and off alternatively along odd and even bonds within each driving period. A comparison between that hybrid quantum circuit and the model introduced in our Sec. II suggests a clear similarity regarding the employed driving protocols. The main differences are that in our case, each qubit is replaced by a lattice site, the coupling bewteen adjacent sites become staggered single-particle hopping, and the non-Hermitian effect is formally introduced by local loss instead of the projective measurements in Ref. [43]. Therefore, upon suitable modifications, an experimental setup that could realize the circuit models in previous studies [43–45] may also be used to realize our model and explore entanglement transitions therein. Besides, as discussed in Appendix B, alternated and reentrant entanglement transitions can appear in our setup even if both intracell and intercell hopping terms are existent in each half of the driving period. The construction of our model thus captures the essential feature of entanglement transitions in a class of non-Hermitian Floquet system with PT symmetry.

In current experiments, periodically quenched non-Hermitian lattices with internal degrees of freedom can be implemented in cold atoms and photonic systems. In cold atoms, the SSH model and its dynamical modulations have been realized through various different strategies [72–75]. For example, in a momentum-space lattice of cold atoms, intracell and intercell hopping terms can be alternatively switched on and off within a quantum-walk scheme [76]. The periodic quenching protocol in our Sec. II could thus be implemented. Furthermore, local loss terms could be introduced by coupling momentum states to an auxiliary momentum-state bath or a different internal state that can be moved away by resonant light [39–42,77–79]. These approaches have been utilized to realize PT-symmetry breaking and nonreciprocal transport in cold atoms. Meanwhile, as discussed in Sec. III, the dynamics of our system is not affected if we only have local loss terms. Putting together, both the driving protocol and non-Hermitian effects of our system should be realizable via non-Hermitian quantum walks of cold atoms in momentum-space lattices, and our model may thus be engineered in such a setup. In photonic systems, 1D arrays of periodically driven resonators have been implemented to detect non-Hermitian Floquet band structures [34]. In parallel with cold-atom quantum walks, photonic quantum walks could also realize alternated switching on and off of intracell and intercell hoppings, together with non-Hermitian effects introduced by polarization-dependent photon loss [29–33]. Photonic setups thus provide another promising candidate for the realization of our Floquet non-Hermitian SSH model and the exploration of its dynamics. Putting together, our system and its entanglement transitions may be experimentally explorable in near-term quantum simulators.

In future work, it would be interesting to consider entanglement phase transitions in non-Hermitian Floquet systems beyond one spatial dimension [80], with impurities or disorder, under other driving protocols, and subject to many-body interactions. Systematic analyses regarding the critical behaviors of steady-state EE at entanglement transition points are highly desired in non-Hermitian Floquet systems. The experimental realization of our quenched non-Hermitian lattice and the detection of entanglement phase transitions therein also constitute interesting directions of future research.

APPENDIX A: STROBOSCOPIC EE AND ITS NUMERICAL CALCULATION

Here we outline an approach that can be used to obtain the stroboscopic EE for our system, which follows the method introduced in Ref. [57]. Compared with the algorithm outlined in the Appendix B of Ref. [57], our difference is just to choose the evolution time interval Δt there as our driving period. This adjustment allows us to find the evolved state only stroboscopically.

In our study, the EE is obtained from a single wave function of noninteracting particles. Following Eqs. (12) and (13), this state vector of our system is given by $|\Psi(t)\rangle = |\Psi(\ell T)\rangle$. The density matrix of the system at any stroboscopic time $t = \ell T$ then reads

$$\rho(t) = |\Psi(t)\rangle\langle\Psi(t)|. \tag{A1}$$

Since $|\Psi(t)\rangle$ is a normalized right state, $\rho(t)$ satisfies the general properties of a pure-state density matrix, i.e., $\rho(t) = \rho^\dagger(t)$, $\rho(t) = \rho^2(t)$, and $\text{Tr}[\rho(t)] = 1$. If we decompose our 1D system into two spatially connected segments X and Y, the reduced density matrix of the subsystem X can be obtained by tracing out all the degrees of freedom belonging to the subsystem Y, i.e.,

$$\rho_X(t) = \text{Tr}_Y[\rho(t)]. \tag{A2}$$

The von Neumann bipartite EE $S(t)$ between the subsystems X and Y is defined in terms of $\rho_X(t)$ as

$$S(t) = -\text{Tr}\{\rho_X(t)\ln[\rho_X(t)]\}. \tag{A3}$$

For free lattice models, a generic connection has been established between the bipartite EE and the spectrum of single-particle correlator [71]. It is irrespective of whether the state evolves following a Hermitian or a non-Hermitian Hamiltonian, so long as we only consider normalized right state vectors. In the lattice representation, the matrix element of single-particle correlator for our system is given by the Eq. (14). By diagonalizing this correlation matrix in the

space of subsystem X, we find the set of its eigenvalues $\{\zeta_j(\ell T)|j = 1, 2, \ldots, 2\ell - 1, 2\ell\}$. Here ℓ is the number of unit cells belonging to the subsystem X, which has 2ℓ sites in total since there are two sublattices within each unit cells. Using these eigenvalues and following Ref. [71], we can obtain the bipartite EE in terms of Eq. (15). Note in passing that our definitions and calculations of EE do not employ biorthogonal state vectors in different Hilbert spaces (see Refs. [81–83] for discussions of the biorthogonal approach), making the recipe of Ref. [71] to be applicable.

The remaining issue is to evaluate the wave function $|\Psi(t)\rangle$ of noninteracting particles and find out the correlation matrix element in Eq. (14) efficiently. Starting with the normalized state $|\Psi(t)\rangle$ [Eq. (12)] at the stroboscopic time $t = \ell T$, we obtain the state after one more evolution period as

$$|\Psi(t + T)\rangle \propto \hat{U}|\Psi(t)\rangle$$

$$= \prod_{n=1}^{N} \left[\sum_{m=1}^{L} \sum_{s=A,B} [e^{-iH_{\text{eff}}}\mathcal{U}]_{msn}(t)\hat{c}^{\dagger}_{m,s} \right] |\emptyset\rangle. \quad (A4)$$

Here N counts the total number of fermions. L is the number of unit cells in the lattice. H_{eff} is a $2L \times 2L$ matrix of the Floquet effective Hamiltonian $\hat{H}_{\text{eff}} \equiv i \ln \hat{U}$ in the lattice representation. The normalized state at $t + T$ can be obtained by performing the QR-decomposition, i.e.,

$$e^{-iH_{\text{eff}}}\mathcal{U} = \mathcal{Q}\mathcal{R}. \quad (A5)$$

Here $\mathcal{Q}$ is a $2L \times N$ matrix satisfying $\mathcal{Q}^{\dagger}\mathcal{Q} = 1$. $\mathcal{R}$ is an $N \times N$ upper triangular matrix. The $2L \times N$ matrix $\mathcal{U}$ is isometry and it also satisfies $\mathcal{U}^{\dagger}\mathcal{U} = 1$. At the time $t + T$, the matrix $\mathcal{U}(t + T)$ is then given by

$$\mathcal{U}(t + T) = \mathcal{Q}. \quad (A6)$$

Note in passing that the matrix $\mathcal{U}(t = 0)$ accounts the initial distribution of fermions in the lattice. For the state $|\Psi_0\rangle$ in Eq. (13), the $\mathcal{U}(t = 0)$ takes the explicit form

$$[\mathcal{U}(0)]_{j,j'} = \delta_{j,2j'}, \qquad j, j' = 1, \ldots, N, \quad (A7)$$

where we have $L = N$ in the half-filled case. Following this approach, we can find the $\mathcal{U}(\ell T)$ at any stroboscopic time $t = \ell T$. The matrix elements of single-particle correlator $C(\ell T)$ can be obtained as

$$C_{ms,m's'}(\ell T) = [\mathcal{U}(\ell T)\mathcal{U}^{\dagger}(\ell T)]_{m's',ms}. \quad (A8)$$

The EE can be finally extracted from the spectrum of $C(\ell T)$ according to Eq. (15) in the main text.

The approach considered here is efficient for studying the long-time stroboscopic dynamics of EE. It is also applicable to both clean and disordered noninteracting fermionic systems and under different boundary conditions. As reported in the main text, our calculations of the Floquet bands and EE give rise to consistent and physically reasonable predictions about the spectrum and entanglement transitions in our system. These can be observed in our Fig. 3 vs Fig. 7 (see also Fig. 4 vs Fig. 8). Such observations offer crosschecks for the correctness and consistency of our dynamical methodology.
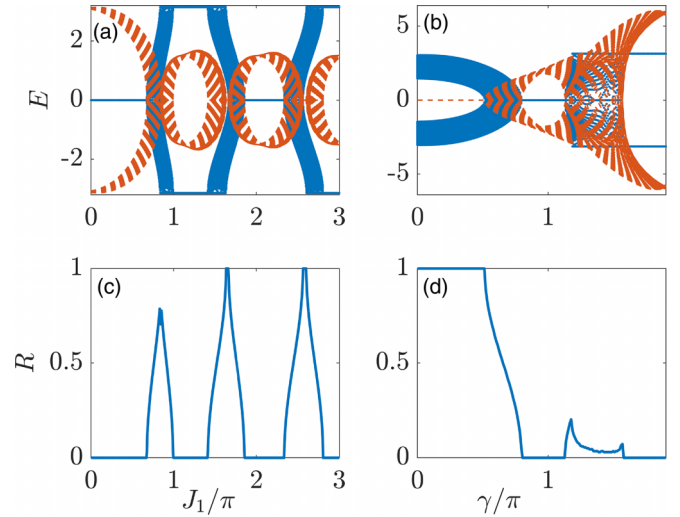

FIG. 9. Floquet spectrum E [(a), (b)] and real-quasienergy ratios R [(c), (d)] of $\hat{U}'$ [Eq. (B4)] vs the hopping amplitude J_1 and gain/loss parameter γ under PBC. We set $J_{10} = J_{20} = \pi/20$ for all panels. Other system parameters are $(J_2, \gamma) = (0.1\pi, 0.5\pi)$ for (a), (c) and $(J_1, J_2) = (2.2\pi, 2\pi/3)$ for (b), (d). The solid points and dashed lines in (a) and (b) denote the real and imaginary parts of quasienergy.

APPENDIX B: ANOTHER DRIVING PROTOCOL

In the main text, we studied a model whose intracell and intercell hopping terms are separately turned on in two different halves of each driving period. This protocol allows us to demonstrate the alternated and reentrant entanglement transitions in non-Hermitian Floquet systems with transpar-
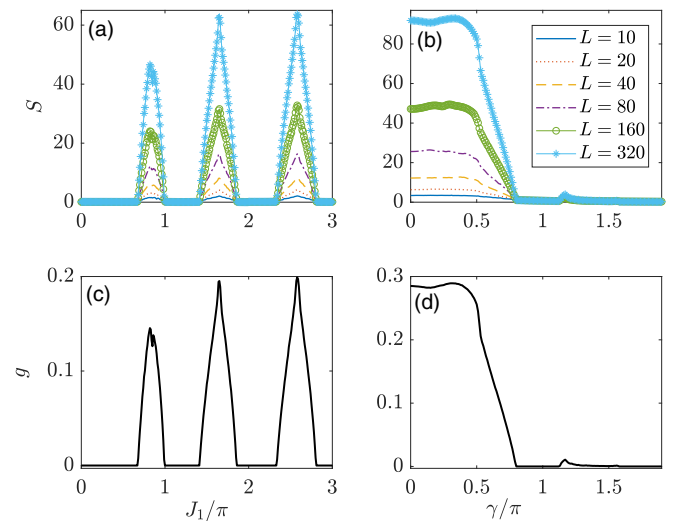

FIG. 10. Reentrant entanglement transitions vs the hopping amplitude J_1 [(a), (c)] and gain/loss strength γ [(b), (d)] of $\hat{U}'$ [Eq. (B4)]. We set $J_{10} = J_{20} = \pi/20$ for all panels. Other system parameters are $(J_2, \gamma) = (0.1\pi, 0.5\pi)$ for (a), (c) and $(J_1, J_2) = (2.2\pi, 2\pi/3)$ for (b), (d). (a) and (b) show the steady-state EE $S(L, l)$, with $l = L/2$, vs J_1 and γ for different lattice sizes L. (c) and (d) show the gradients g extracted from the linear fitting $S(L, L/2) \sim gL + s_0$ of EE.

ent theoretical and numerical analyses. In this Appendix, we showcase that the phenomena reported in the main text are not restricted to the piecewise quenching protocol considered there.

As an example, we consider a situation in which both the intracell and intercell hopping terms are present throughout each driving period. The time-dependent Hamiltonian now takes the form

$$\hat{H}'(t) = \begin{cases} \hat{H}'_1 & t \in [\ell T, \ell T + T/2), \\ \hat{H}'_2 & t \in [\ell T + T/2, \ell T + T), \end{cases} \quad \text{(B1)}$$

where $\hat{H}'_1 = \hat{H}_1 + \hat{H}_{10}$ and $\hat{H}'_2 = \hat{H}_2 + \hat{H}_{20}$. $\hat{H}_1$ and $\hat{H}_2$ are Hamiltonians given by the Eqs. (2) and (3) in the main text. The additional terms read

$$\hat{H}_{10} = J_{10} \sum_n (\hat{c}^\dagger_{n,B} \hat{c}_{n+1,A} + \text{H.c.}), \quad \text{(B2)}$$

$$\hat{H}_{20} = J_{20} \sum_n (\hat{c}^\dagger_{n,A} \hat{c}_{n,B} + \text{H.c.}). \quad \text{(B3)}$$

The system now possesses intracell and intercell hopping with amplitudes J_1 and J_{10} (J_{20} and J_2) in the first (second) half of each driving period. The Floquet operator of this model is given by

$$\hat{U}' = e^{-i\hat{H}'_2} e^{-i\hat{H}'_1}. \quad \text{(B4)}$$

Following the methods of Sec. II, we obtain the spectra and real-quasienergy ratios of the system described by the Floquet operator $\hat{U}'$ [Eq. (B4)], as reported in Fig. 9. We find that with the variation of J_1, there are also alternated transitions between real and complex Floquet spectra. Moreover, reentrant transitions from complex to partially real Floquet spectra are observed with the increase of γ. The spectrum features of our Floquet model considered in the main text can thus be qualitatively reproduced after adding the intercell and intracell hopping terms contained in $\hat{H}_{10}$ and $\hat{H}_{20}$.

Referring to the approaches outlined in Sec. III and Appendix A, we obtain the steady-state EE $S(L, L/2)$ from the dynamics guided by $\hat{U}'$ [Eq. (B4)] for different L, and further extracting its scaling law vs L at different hopping and non-Hermitian parameters J_1 and γ [Eq. (B4)]. As shown in Fig. 10, alternated and reentrant entanglement transitions are clearly observed, and their features are qualitatively identical to those presented in the Fig. 7 for our original model $\hat{U}$.

Therefore, we conclude that the rich and unique features of spectrum and entanglement transitions in our non-Hermitian Floquet system could emerge under different quenching protocols (here with either $J_{10} = J_{20} = 0$ or $J_{10}, J_{20} \neq 0$). It remains an interesting issue to explore other types of Floquet entanglement transitions under different classes of periodic driving fields (e.g., harmonic, delta-kicking) in future studies.

[1] L. Zhou and D. Zhang, Non-Hermitian Floquet topological matter—a review, Entropy **25**, 1401 (2023).

[2] J. Gong and Q.-h. Wang, Stabilizing non-Hermitian systems by periodic driving, Phys. Rev. A **91**, 042135 (2015).

[3] C. Yuce, PT symmetric Floquet topological phase, Eur. Phys. J. D **69**, 184 (2015).

[4] L. Zhou and J. Gong, Non-Hermitian Floquet topological phases with arbitrarily many real-quasienergy edge states, Phys. Rev. B **98**, 205417 (2018).

[5] Z. Turker, S. Tombuloglu, and C. Yuce, PT symmetric Floquet topological phase in SSH model, Phys. Lett. A **382**, 2013 (2018).

[6] L. Zhou and J. Pan, Non-Hermitian Floquet topological phases in the double-kicked rotor, Phys. Rev. A **100**, 053608 (2019).

[7] L. Zhou, Dynamical characterization of non-Hermitian Floquet topological phases in one dimension, Phys. Rev. B **100**, 184314 (2019).

[8] J. Pan and L. Zhou, Non-Hermitian Floquet second order topological insulators in periodically quenched lattices, Phys. Rev. B **102**, 094305 (2020).

[9] L. Zhou, Non-Hermitian Floquet phases with even-integer topological invariants in a periodically quenched two-leg ladder, Entropy **22**, 746 (2020).

[10] X. Zhang and J. Gong, Non-Hermitian Floquet topological phases: Exceptional points, coalescent edge modes, and the skin effect, Phys. Rev. B **101**, 045415 (2020).

[11] H. Wu and J. An, Floquet topological phases of non-Hermitian systems, Phys. Rev. B **102**, 041119(R) (2020).

[12] L. Zhou, Y. Gu, and J. Gong, Dual topological characterization of non-Hermitian Floquet phases, Phys. Rev. B **103**, L041404 (2021).

[13] Y. Cao, Y. Li, and X. Yang, Non-Hermitian bulk-boundary correspondence in a periodically driven system, Phys. Rev. B **103**, 075126 (2021).

[14] S. Wu, W. Song, S. Gao, Y. Chen, S. Zhu, and T. Li, Floquet π mode engineering in non-Hermitian waveguide lattices, Phys. Rev. Res. **3**, 023211 (2021).

[15] V. M. Vyas and D. Roy, Topological aspects of periodically driven non-Hermitian Su-Schrieffer-Heeger model, Phys. Rev. B **103**, 075441 (2021).

[16] C.-H. Liu, H. Hu, and S. Chen, Symmetry and topological classification of Floquet non-Hermitian systems, Phys. Rev. B **105**, 214305 (2022).

[17] W. Zhu and J. Gong, Hybrid skin-topological modes without asymmetric couplings, Phys. Rev. B **106**, 035425 (2022).

[18] L. Zhou, R. W. Bomantara, and S. Wu, qth-root non-Hermitian Floquet topological insulators, SciPost Phys. **13**, 015 (2022).

[19] M. van Caspel, S. E. T. Arze, and I. P. Castillo, Dynamical signatures of topological order in the driven-dissipative Kitaev chain, SciPost Phys. **6**, 026 (2019).

[20] L. Zhou, Non-Hermitian Floquet topological superconductors with multiple Majorana edge modes, Phys. Rev. B **101**, 014306 (2020).

[21] A. K. Ghosh and T. Nag, Non-Hermitian higher-order topological superconductors in two dimensions: Statics and dynamics, Phys. Rev. B **106**, L140303 (2022).

[22] P. He and Z. Huang, Floquet engineering and simulating exceptional rings with a quantum spin system, Phys. Rev. A **102**, 062201 (2020).

[23] A. Banerjee and A. Narayan, Controlling exceptional points with light, Phys. Rev. B **102**, 205423 (2020).

[24] D. Chowdhury, A. Banerjee, and A. Narayan, Light-driven Lifshitz transitions in non-Hermitian multi-Weyl semimetals, Phys. Rev. A **103**, L051101 (2021).

[25] D. Chowdhury, A. Banerjee, and A. Narayan, Exceptional hexagonal warping effect in multi-Weyl semimetals, Phys. Rev. B **105**, 075133 (2022).

[26] H. Wu and J.-H. An, Non-Hermitian Weyl semimetal and its Floquet engineering, Phys. Rev. B **105**, L121113 (2022).

[27] L. Zhou, Floquet engineering of topological localization transitions and mobility edges in one-dimensional non-Hermitian quasicrystals, Phys. Rev. Res. **3**, 033184 (2021).

[28] L. Zhou and W. Han, Driving-induced multiple $\mathscr{PT}$-symmetry breaking transitions and reentrant localization transitions in non-Hermitian Floquet quasicrystals, Phys. Rev. B **106**, 054307 (2022).

[29] J. M. Zeuner, M. C. Rechtsman, Y. Plotnik, Y. Lumer, S. Nolte, M. S. Rudner, M. Segev, and A. Szameit, Observation of a topological transition in the bulk of a non-Hermitian system, Phys. Rev. Lett. **115**, 040402 (2015).

[30] X. Zhan, L. Xiao, Z. Bian, K. Wang, X. Qiu, B. C. Sanders, W. Yi, and P. Xue, Detecting topological invariants in nonunitary discrete-time quantum walks, Phys. Rev. Lett. **119**, 130501 (2017).

[31] T. Nitsche, S. Barkhofen, R. Kruse, L. Sansoni, M. Štefaňák, A. Gábris, V. Potoček, T. Kiss, I. Jex, and C. Silberhorn, Probing measurement-induced effects in quantum walks via recurrence, Sci. Adv. **4**, eaar6444 (2018).

[32] S. Weidemann, M. Kremer, S. Longhi, and A. Szameit, Topological triple phase transition in non-Hermitian Floquet quasicrystals, Nature (London) **601**, 354 (2022).

[33] Q. Lin, T. Li, L. Xiao, K. Wang, W. Yi, and P. Xue, Topological phase transitions and mobility edges in non-Hermitian quasicrystals, Phys. Rev. Lett. **129**, 113601 (2022).

[34] J. Park, H. Cho, S. Lee, K. Lee, K. Lee, H. C. Park, J.-W. Ryu, N. Park, S. Jeon, and B. Min, Revealing non-Hermitian band structure of photonic Floquet media, Sci. Adv. **8**, eabo6220 (2022).

[35] Z. Gu, H. Gao, H. Xue, J. Li, Z. Su, and J. Zhu, Transient non-Hermitian skin effect, Nat. Commun. **13**, 7668 (2022).

[36] H. Gao, H. Xue, Z. Gu, L. Li, W. Zhu, Z. Su, J. Zhu, B. Zhang, and Y. D. Chong, Anomalous Floquet non-Hermitian skin effect in a 1612 ring resonator lattice, Phys. Rev. B **106**, 134112 (2022).

[37] Y. Huang, Z. Yin, and W. Yang, Realizing a topological transition in a non-Hermitian quantum walk with circuit QED, Phys. Rev. A **94**, 022302 (2016).

[38] M. Chitsazi, H. Li, F. M. Ellis, and T. Kottos, Experimental realization of floquet $\mathcal{PT}$-symmetric systems, Phys. Rev. Lett. **119**, 093901 (2017).

[39] J. Li, A. K. Harter, J. Liu, L. d. Melo, Y. N. Joglekar and L. Luo, Observation of parity-time symmetry breaking transitions in a dissipative Floquet system of ultracold atoms, Nat. Commun. **10**, 855 (2019).

[40] W. Gou, T. Chen, D. Xie, T. Xiao, T. Deng, B. Gadway, W. Yi, and B. Yan, Tunable nonreciprocal quantum transport through a dissipative aharonov-bohm ring in ultracold atoms, Phys. Rev. Lett. **124**, 070402 (2020).

[41] T. Chen, W. Gou, D. Xie, T. Xiao, W. Yi, J. Jing, and B. Yan, Quantum Zeno effects across a parity-time symmetry breaking transition in atomic momentum space, npj Quantum Inf. **7**, 78 (2021).

[42] Q. Liang, D. Xie, Z. Dong, H. Li, H. Li, B. Gadway, W. Yi, and B. Yan, Dynamic signatures of non-Hermitian skin effect and topology in ultracold atoms, Phys. Rev. Lett. **129**, 070401 (2022).

[43] Y. Li, X. Chen, and M. P. A. Fisher, Quantum zeno effect and the many-body entanglement transition, Phys. Rev. B **98**, 205136 (2018).

[44] B. Skinner, J. Ruhman, and A. Nahum, Measurement-induced phase transitions in the dynamics of entanglement, Phys. Rev. X **9**, 031009 (2019).

[45] A. Chan, R. M. Nandkishore, M. Pretko, and G. Smith, Unitary-projective entanglement dynamics, Phys. Rev. B **99**, 224307 (2019).

[46] Y. Li, X. Chen, and M. P. A. Fisher, Measurement-driven entanglement transition in hybrid quantum circuits, Phys. Rev. B **100**, 134306 (2019).

[47] X. Cao, A. Tilloy, and A. D. Luca, Entanglement in a fermion chain under continuous monitoring, SciPost Phys. **7**, 024 (2019).

[48] C. Noel, P. Niroula, D. Zhu, A. Risinger, L. Egan, D. Biswas, M. Cetina, A. V. Gorshkov, M. J. Gullans, D. A. Huse, and C. Monroe, Measurement-induced quantum phases realized in a trapped-ion quantum computer, Nat. Phys. **18**, 760 (2022).

[49] J. M. Koh, S.-N. Sun, M. Motta, and A. J. Minnich, Measurement-induced entanglement phase transition on a superconducting quantum processor with mid-circuit readout, Nat. Phys. **19**, 1314 (2023).

[50] Google Quantum AI and Collaborators, Measurement-induced entanglement and teleportation on a noisy quantum processor, Nature (London) **622**, 481 (2023).

[51] A. C. Potter and R. Vasseur, Entanglement Dynamics in Hybrid Quantum Circuits, in *Entanglement in Spin Chains, Quantum Science and Technology*, edited by A. Bayat, S. Bose, and H. Johannesson (Springer, Cham, 2022).

[52] M. P. A. Fisher, V. Khemani, A. Nahum, and S. Vijay, Random quantum circuits, Annu. Rev. Condens. Matter Phys. **14**, 335 (2023).

[53] B. Skinner, Lecture Notes: Introduction to random unitary circuits and the measurement-induced entanglement phase transition, arXiv:2307.02986.

[54] Á. Bácsi and B. Dóra, Dynamics of entanglement after exceptional quantum quench, Phys. Rev. B **103**, 085137 (2021).

[55] S. Gopalakrishnan and M. J. Gullans, Entanglement and purification transitions in non-Hermitian quantum mechanics, Phys. Rev. Lett. **126**, 170503 (2021).

[56] X. Turkeshi, M. Dalmonte, R. Fazio, and M. Schirò, Entanglement transitions from stochastic resetting of non-Hermitian quasiparticles, Phys. Rev. B **105**, L241114 (2022).

[57] K. Kawabata, T. Numasawa, and S. Ryu, Entanglement phase transition induced by the non-Hermitian skin effect, Phys. Rev. X **13**, 021007 (2023).

[58] E. Granet, C. Zhang, and H. Dreyer, Volume-law to area-law entanglement transition in a nonunitary periodic Gaussian circuit, Phys. Rev. Lett. **130**, 230401 (2023).

[59] Y. Le Gal, X. Turkeshi and M. Schirò, Volume-to-area law entanglement transition in a non-Hermitian free fermionic chain, SciPost Phys. **14**, 138 (2023).

[60] X. Turkeshi and M. Schiró, Entanglement and correlation spreading in non-Hermitian spin chains, Phys. Rev. B **107**, L020403 (2023).

[61] K. Li, Z.-C. Liu, and Y. Xu, Disorder-induced entanglement phase transitions in non-Hermitian systems with skin effects, arXiv:2305.12342.

[62] L. Zhou, Entanglement phase transitions in non-Hermitian quasicrystals, Phys. Rev. B **109**, 024204 (2024).

[63] S. Li, X. Yu, and Z. Li, Emergent entanglement phase transitions in non-Hermitian Aubry-André-Harper chains, Phys. Rev. B **109**, 024306 (2024).

[64] W. P. Su, J. R. Schrieffer, and A. J. Heeger, Solitons in polyacetylene, Phys. Rev. Lett. **42**, 1698 (1979).

[65] W. P. Su, J. R. Schrieffer, and A. J. Heeger, Soliton excitations in polyacetylene, Phys. Rev. B **22**, 2099 (1980).

[66] A. U. Hassan, B. Zhen, M. Soljačić, M. Khajavikhan, and D. N. Christodoulides, Dynamically encircling exceptional points: Exact evolution and polarization state conversion, Phys. Rev. Lett. **118**, 093002 (2017).

[67] S. Lieu, Non-Hermitian Majorana modes protect degenerate steady state, Phys. Rev. B **100**, 085110 (2019).

[68] N. Matsumoto, K. Kawabata, Y. Ashida, S. Furukawa, and M. Ueda, Continuous phase transition without gap closing in non-Hermitian quantum many-body systems, Phys. Rev. Lett. **125**, 260601 (2020).

[69] A. Panda and S. Banerjee, Entanglement in nonequilibrium steady states and many-body localization breakdown in a current-driven system, Phys. Rev. B **101**, 184201 (2020).

[70] S. Longhi, Phase transitions and bunching of correlated particles in a non-Hermitian quasicrystal, Phys. Rev. B **108**, 075121 (2023).

[71] I. Peschel and V. Eisler, Reduced density matrices and entanglement entropy in free lattice models, J. Phys. A: Math. Theor. **42**, 504003 (2009).

[72] M. Atala, M. Aidelsburger, J. T. Barreiro, D. Abanin, T. Kitagawa, E. Demler, and I. Bloch, Direct measurement of the Zak phase in topological Bloch bands, Nat. Phys. **9**, 795 (2013).

[73] E. J. Meier, F. A. An, and B. Gadway, Observation of the topological soliton state in the Su-Schrieffer-Heeger model, Nat. Commun. **7**, 13986 (2016).

[74] D. Xie, W. Gou, T. Xiao, B. Gadway, and B. Yan, Topological characterizations of an extended Su-Schrieffer-Heeger model, npj Quantum Inf. **5**, 55 (2019).

[75] S. K. Kanungo, J. D. Whalen, Y. Lu, M. Yuan, S. Dasgupta, F. B. Dunning, K. R. A. Hazzard, and T. C. Killian, Realizing topological edge states with Rydberg-atom synthetic dimensions, Nat. Commun. **13**, 972 (2022).

[76] T. Xiao, D. Xie, W. Gou, T. Chen, T. Deng, W. Yi, and B. Yan, Periodic driving induced helical Floquet channels with ultracold atoms in momentum space, Eur. Phys. J. D **74**, 152 (2020).

[77] Y. Xu, S. Wang, and L. Duan, Weyl exceptional rings in a three-dimensional dissipative cold atomic gas, Phys. Rev. Lett. **118**, 045701 (2017).

[78] S. Lapp, J. Ang'ong'a, F. A. An, and B. Gadway, Engineering tunable local loss in a synthetic lattice of momentum states, New J. Phys. **21**, 045006 (2019).

[79] Z. Ren, D. Liu, E. Zhao, C. He, K. K. Pak, J. Li, and G.-B. Jo, Chiral control of quantum states in non-Hermitian spin-orbit-coupled fermions, Nat. Phys. **18**, 385 (2022).

[80] Dmitry S. Ageev, Andrey A. Bagrov, and Askar A. Iliasov, Deterministic chaos and fractal entropy scaling in Floquet conformal field theories, Phys. Rev. B **103**, L100302 (2021).

[81] R. Couvreur, J. L. Jacobsen, and H. Saleur, Entanglement in nonunitary quantum critical spin chains, Phys. Rev. Lett. **119**, 040601 (2017).

[82] L. Herviou, J. H. Bardarson, and N. Regnault, Defining a bulk-edge correspondence for non-Hermitian hamiltonians via singular-value decomposition, Phys. Rev. A **99**, 052118 (2019).

[83] P.-Y. Chang, J.-S. You, X. Wen, and S. Ryu, Entanglement spectrum and entropy in topological non-Hermitian systems and nonunitary conformal field theory, Phys. Rev. Res. **2**, 033069 (2020).